A Wave Optics Based Fiber Scattering Model

MENGQI (MANDY) XIA, Cornell University
BRUCE WALTER, Cornell University
ERIC MICHIELSSEN, University of Michigan
DAVID BINDEL, Cornell University
STEVE MARSCHNER, Cornell University

Fig. 1. We present the first wave optics based fiber scattering model. We use a 2.5D method, where the geometry is specified using its 2D cross section while the wave fields are 3D. Our wave-simulation-based azimuthal scattering functions are combined with conventional longitudinal functions to create BCSDFs for rendering. Our new model is able to produce diffraction and interference effects that cannot be captured by previous ray-based models. This figure shows a spiderweb iridescence example. (a) is a photograph of this effect by Marianna Armata [2019a; 2019b]. (b) is rendered using our wave-based BCSDF and (c) is rendered using a previous ray-based BCSDF. Our wave optics fiber scattering model is able to produce strong color effects with hues similar to the photograph while the ray model produces a colorless appearance. Similar iridescence effects can also be seen in eyelashes or a Dandelion seed head [Wall 2011].

Existing fiber scattering models in rendering are all based on tracing rays through fiber geometry, but for small fibers diffraction and interference are non-negligible, so relying on ray optics can result in appearance errors. This paper presents the first wave optics based fiber scattering model, introducing an azimuthal scattering function that comes from a full wave simulation. Solving Maxwell's equations for a straight fiber of constant cross section illuminated by a plane wave reduces to solving for a 3D electromagnetic field in a 2D domain, and our fiber scattering simulator solves this 2.5D problem efficiently using the boundary element method (BEM). From the resulting fields we compute extinction, absorption, and far-field scattering distributions, which we use to simulate shadowing and scattering by fibers in a path tracer. We validate our path tracer against the wave simulation and the simulation against a measurement of diffraction from a single textile fiber. Our results show that our approach can reproduce a wide range of fibers with different sizes, cross sections, and material properties, including textile fibers, animal fur, and human hair. The renderings include color effects, softening of sharp features, and strong forward scattering that are not predicted by traditional ray-based models, though the two approaches produce similar appearance for complex fiber assemblies under many conditions.

Authors' addresses: Mengqi (Mandy) Xia, Cornell University; Bruce Walter, Cornell University; Eric Michielssen, University of Michigan; David Bindel, Cornell University; Steve Marschner, Cornell University.

1 INTRODUCTION

Most computer graphics assumes that light travels as rays. When objects are sufficiently large compared to visible light wavelengths, ray optics is a good approximation that is accurate enough for most relevant appearance effects. Wave optics provides an alternative model that characterizes light as an electromagnetic wave that obeys Maxwell's equations, which is more accurate at all scales. Wave optics is important for simulating light interaction with small objects, but is more difficult to compute.

Light scattering from fibers is important for rendering textiles, animal fur, and human hair in visual effects and other applications.

By definition fibers are very thin, and though many successful models for fiber scattering have been built with ray optics, the scale of many types of fibers, especially textile fibers and animal fur fibers, calls the accuracy of this approach into question.

In this paper, we propose a new fiber scattering model that is built on wave optics simulation, and we study the differences between its predictions and those of conventional ray-based models. To the best of our knowledge, this is the first wave optics fiber scattering model in computer graphics.

Conducting full wave scattering simulations is expensive, as it requires resolving both electromagnetic fields and geometry at well below the scale of visible light wavelengths. Furthermore, creating a complete scattering model requires many simulations to account for all possible illumination directions. This paper shows a way to make this computation tractable through a series of simplifications:

- Like most fiber scattering models we assume a separable form for the model, as a product of longitudinal and azimuthal scattering distributions, and in this paper we work only on the azimuthal distribution, adopting a longitudinal model from prior work [d'Eon et al. 2011].
- For modeling azimuthal scattering we assume that fibers are extrusions with perfect translational symmetry. We exploit this symmetry in a "2.5D" wave scattering simulation that computes 3D electromagnetic fields using values only in a 2D cross-sectional slice.
- To avoid the need to discretize the volume of the fiber and the space surrounding it, we employ a boundary integral formulation that reduces the set of unknowns to a 1D discretization of the fiber's planar cross section curve.

With careful attention to efficiency in implementation, this makes it possible to compute azimuthal scattering for fibers of arbitrary cross sections and arbitrary material properties, for all incident and scattered directions and all relevant wavelengths, in a precomputation, resulting in tabulated azimuthal scattering functions to be used in rendering.

The following sections detail our techniques (Sections 4, 5, 6), their validation (Section 6), and the simulation and rendering results (Section 8). We confirm our simulation against prior implementations, verify that rendering a single-fiber scene matches the simulation results, and provide a simple validation against measurement. We examine the differences and similarities between the results of ray and wave models, and the renders show a reassuringly good match for larger fibers at most angles, substantial differences in color and highlight shapes for smaller fibers and complex cross section shapes, and dramatically stronger forward scattering in the wave model.

1.1 Assumptions and limitations

Building a truly complete, general, and practical wave-based fiber scattering model is a major undertaking, and this first model comes with several limitations.

- Like most fiber models, we assume the scattering function can be factored into the product of an azimuthal scattering function and a longitudinal scattering function. However, since the wave simulation has no notion of separation into different scattering modes, we use a single longitudinal distribution, so our model does not include effects from structural asymmetries like the cuticle scales in human hair.
- Our model is for the far field and does not account for incident light that varies across the width of a fiber or views where individual fibers are wider than pixels. The simulation results do contain this information but it is not carried over to the renderer.
- Path tracing assumes that scattering from different fibers can be treated independently and we maintain that assumption, potentially leaving out effects due to interference between light scattered coherently by different fibers.
- Although our simulator handles arbitrary polarization, for simplicity of integrating the new scattering model into current rendering systems we assume light incident on a fiber is always unpolarized.

2 RELATED WORK

Before discussing how we apply wave optics to develop a wave-based fiber scattering model, we will first review the conventional ray-based fiber scattering functions, previous wave-based reflectance models in Computer Graphics, and the computational electromagnetics tools that are available for this problem.

Fiber scattering models. Marschner et al. [2003] introduced a hair scattering model based on a dielectric cylinder, which represents the scattering function as a sum of the R, TT and TRT lobes and factors each lobe into the product of an azimuthal scattering function and a longitudinal function. Their model improved on previous models in matching measurements and is widely used. Following this work, Zinke and Weber [2007] formalized the notion of Bidirectional Curve Scattering Distribution Function (BCSDF) and proposed a near-field model (an approach adopted later adopted by Chiang et al. [2015] for its speed).

Zinke et al. [2009] added a diffuse component to the model so that it better matches measurements and Sadeghi et al. [2010] adapted the model to be more artist friendly. d'Eon et al. [2011] fixed an energy conservation problem with Marschner's model by introducing an elegant new longitudinal component and an azimuthal component based on numerical quadrature. Later, d'Eon et al. [2014] proposed a non-separable reflectance lobe by making the longitudinal distribution dependent on relative azimuth.

Fiber scattering models are also essential for realistic fur rendering. Yan et al. [2017, 2015] introduced a double cylinder model that models the medulla in the interior of fibers to better match animal fur appearance.

Azimuthal variations are important to fiber appearance. Khungurn and Marschner [2017] proposed a new azimuthal scattering function for elliptical hair fibers, revealing optical and appearance differences compared to circular fibers. Aliaga et al. [2017] introduced a new fiber scattering model specifically for textile fibers. They ray traced different textile fiber shapes, using measured material properties, to precompute scattering functions. Both of these methods used a tabular approach to represent fiber scattering, as our work also does.

Fiber scattering is also studied in the Applied Physics community. Linder [2014] studied circular cylinder scattering using the Mie solution. They simulated scattering media consisting of such cylinders using a Monte Carlo framework and applied their results to analyze scattering by paper fibers. Similar to our work, they also observed strong forward scattering. However, their work only considers circular cylinders while our work is for general cross-section shapes.

Wave optics reflectance models. Wave optics has been used extensively for rough surface reflectance modeling. For example, models have been developed for surfaces with random [He et al. 1991] or periodic [Stam 1999] stationary statistics, and for predicting average [Dong et al. 2016] and fine-scale appearance [Yan et al. 2018] for surfaces with known geometric microstructures. These surface models used variants of either the Beckmann-Kirchoff [Beckmann and Spizzichino 1987] or Harvey-Shack [Harvey 1979] scattering approximations. Werner et al. [2017] proposed a model based on non-paraxial scalar diffraction theory to render scratch iridescence. Toisoul and Ghosh [2017] proposed a measurement method and a data-driven rendering approach to render complex diffraction effects in real-time. While more tractable, these scalar wave approximations are less accurate for highly non-planar geometry and neglect multiple scattering, making them unsuitable for simulating fiber scattering. In our work, we use full vector wave simulations, which are more accurate.

Thin-film interference produces colorful iridescence; Smits and Meyer [1992] and Gondek et al. [1994] built early models for iridescent specular BRDFs, and Belcour and Barla [2017] extended the Microfacet model to incorporate thin-film iridescence. They proposed a preintegration scheme for the spectral dimension to preserve efficiency while preventing color artifacts from spectral aliasing. Our azimuthal results can similarly oscillate rapidly as a function of wavelength. However, since they are not in analytic form, no simple preintegration method is available, and instead we densely sample the spectral dimension.

Wave optics in volume scattering has also been studied in the Graphics community [Bar et al. 2019; Frisvad et al. 2007; Sadeghi et al. 2010]. In comparison, our work focuses on a different type of particles: cylindrical particles, and handles arbitrary cross sections by full wave simulation.

The most detailed previous wave optics work in graphics used finite-difference time-domain (FDTD) simulations of periodic microstructures of butterfly wings [Musbach et al. 2013]. FDTD requires finely discretizing an enclosing 3D volume, which limits the feasible problem size. In contrast, our work uses the boundary element method (BEM), which only discretizes the boundary of the scatterer and scales better to handle our larger geometries.

Computational electromagnetics. Computational electromagnetics (CEM) is a discipline that develops computational methods to understand electromagnetic phenomena, and it applies to optics since light is an electromagnetic wave. The most frequently used algorithms in CEM are the finite-difference time-domain (FDTD) method, the finite element method (FEM), and the boundary element method (BEM), which is also referred to as the method of moments (MoM) [Rylander et al. 2012]. FDTD [Kane Yee 1966; Taflove and
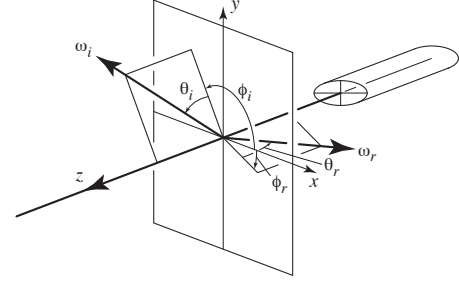

Fig. 2. An illustration of the commonly adopted longitudinal-azimuthal parameterization for fiber scattering models. Each of the directions ω_i and ω_r in 3D is parameterized using the polar angle θ, defined as the angle between ω and the plane perpendicular to the cylinder axis, and the azimuthal angle ϕ, defined in that plane.

Hagness 2005] solves the differential form of Maxwell's equations on a structured grid of points. The advantage of FDTD is that the discretization is straightforward and implementation is relatively easy. However, FDTD is not as flexible as the other two methods as it only works on Cartesian grids [Kunz and Luebbers 1993]. FEM can also be used to solve the time-domain problem, and it works much better for complex geometry, but both FDTD and FEM require discretizing the entire 3D space.

BEM [Huddleston et al. 1986; Wu and Tsai 1977] reformulates the problem in the frequency domain into an integral equation on the scattering surface, then solves this lower dimensional problem using finite elements. Similar to FEM, BEM also handles complex geometry well, and the main advantage of BEM is the low number of unknowns as we only need to solve unknowns on the boundary of the scatterers. In this work, we project from 3D to 2D, then use BEM on a discretization of the 1D contour of the fiber cross section.

3 BACKGROUND

3.1 Fiber scattering models

Fiber scattering models, used to render hair, fur and cloth fibers, usually represent individual fibers as cylinders and use the Bidirectional Curve Scattering Distribution Function (BCSDF) to characterize the scattering properties of a fiber. Similar to the BSDF, it describes outgoing radiance L_r as an integration of incident radiance L_i multiplied by the BCSDF S:

$$L_r(\omega_r, \lambda) = \int L_i(\omega_i, \lambda) \, S(\omega_i, \omega_r, \lambda) \cos\theta_i \mathrm{d}\omega_i. \qquad (1)$$

We will write the BCSDF in spherical coordinates as $S(\theta_i, \theta_r, \phi_i, \phi_r, \lambda)$ using the angles illustrated in Figure 2. Many models write the BCSDF as a sum of reflective and transmissive modes S_p, with each mode S_p factored into a longitudinal function M_p and an azimuthal function N_p. In this work, we assume a single longitudinal function M_0:

$$S(\theta_i, \theta_r, \phi_i, \phi_r, \lambda) = M_0(\theta_i, \theta_r) \sum_{p=0}^{\infty} N_p(\theta_i, \phi_i, \phi_r, \lambda) \qquad (2)$$

We discuss the generalization to full 3D geometry, which would remove this assumption, in Section 9. Our main contribution is a
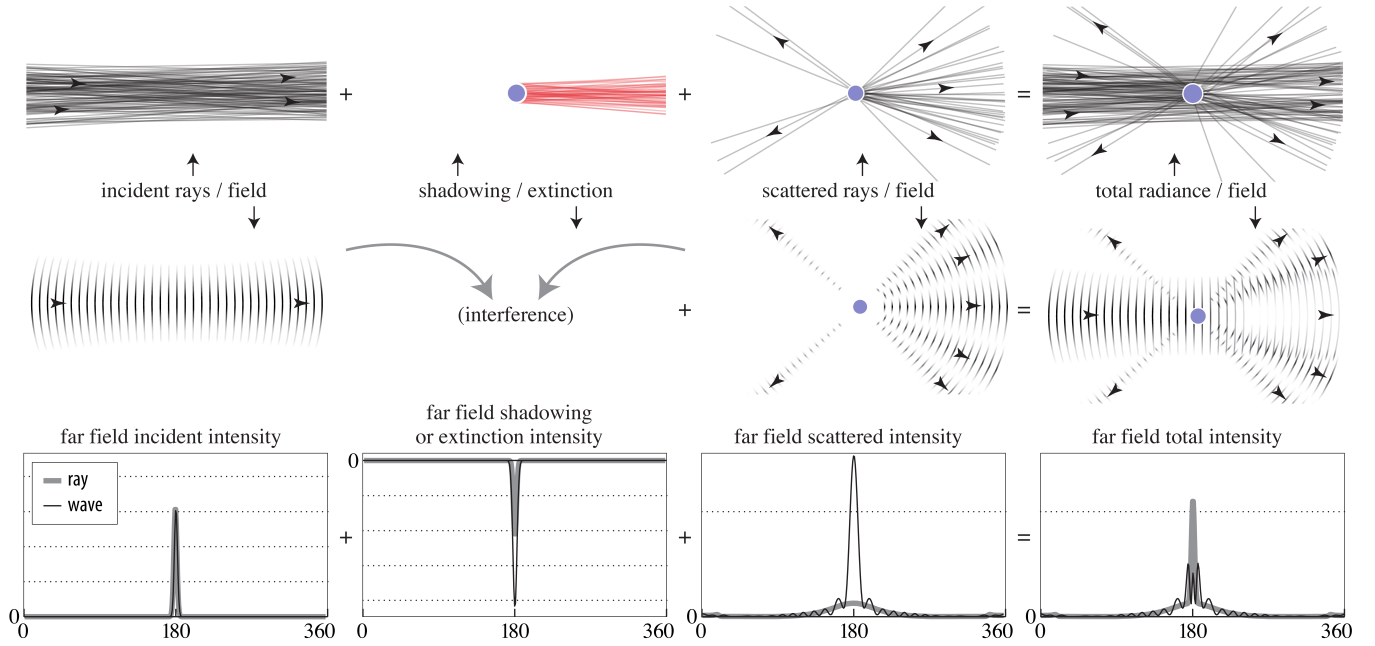
Fig. 3. An overview of fiber scattering in ray and wave optics. Top: in ray optics, introducing the fiber into a beam causes some rays to be blocked (shadowing) and the blocked rays to be redirected (scattering). Middle: in wave optics, introducing the fiber produces a scattered field which adds with the incident field; the analogous effect to shadowing, known as extinction, is caused by interference between these fields. Bottom: far-field intensity simulated using the two models for a Gaussian beam normally incident on a circular fiber; the incident distributions match, but extinction (a measurement of intensity lost to interference) removes more power from the beam than shadowing, and wave scattering redistributes this energy as stronger scattering in near-forward directions.

new azimuthal function $N_{\text{wave}}(\theta_i, \phi_i, \phi_r, \lambda)$ that is fully wave optics based, which replaces the sum of azimuthal lobes; that is:

$$N_{\text{ray}}(\theta_i, \phi_i, \phi_r, \lambda) = \sum_{p=0}^{\infty} N_p(\theta_i, \phi_i, \phi_r, \lambda) \approx N_{\text{wave}}(\theta_i, \phi_i, \phi_r, \lambda). \quad (3)$$

We adopt the longitudinal scattering function M_0 of d'Eon et al. [2011], which guarantees energy conservation.

3.2 Differences between ray- and wave-based models

The ray and wave viewpoints have fundamental differences that lead to challenges in integrating a wave solution into a path tracer. In both theories, the process of scattering from a fiber begins with incident illumination, and introducing the object causes far-field intensity in some directions to decrease and in other directions to increase, but both the distribution and overall magnitude of the change are different, as well as the mechanism (Figure 3).

In ray optics, the incident illumination is a light field, assigning a radiance to each ray passing through the domain. Introducing the fiber causes shadowing as some rays are blocked, and scattering as light is redirected to other rays. The effect on the far-field distribution is found by integrating across the fiber width to produce a shadowing intensity that subtracts from the far-field intensity and a scattering intensity that adds to it.

Scattered intensity integrates to the total power (per unit length understood throughout this section) scattered by the fiber, and shadowing intensity integrates to the total power incident on the fiber; the difference between these is the power absorbed by the fiber.

In wave optics, the incident illumination is a wave field, a complex-valued function of space that satisfies the time-harmonic Maxwell's equations. Introducing the fiber adds another region with different material properties and causes the fields to change. The fields we observe before/after introducing the scatterer are the incident/total fields; the difference between the total and incident fields is an outward-propagating wave field called the scattered field. Each field has a far-field intensity distribution, but due to interference, the total intensity is not just the sum of the incident and scattered intensities.

The difference between the total field intensity and the sum of incident and scattered field intensity can be readily computed from the fields, and we call it the extinction intensity. The extinction intensity and scattered intensity can each be integrated to find the total extinction power and total scattered power. The total extinction might be greater than or less than the total shadowing computed by the ray model.

The results of a wave simulation are in terms of extinction and scattered intensity, whereas scattering from a fiber in a path tracer operates by shadowing the incident rays and introducing scattered rays. Extinction plays a role analogous to shadowing; both describe the total amount of radiant power that interacts with the fiber. But there is a problem: the total extinction does not match the total

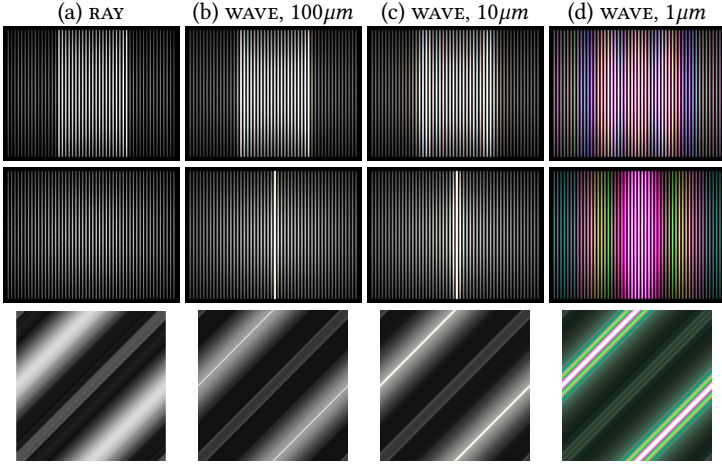(a) RAY   (b) WAVE, $100\mu m$ (c) WAVE, $10\mu m$ (d) WAVE, $1\mu m$

Fig. 4. We compare renders of one layer of aligned circular white fibers lit by a point source. In the first row, the light is close to the camera; in the second row, the light behind the fiber layer and on the centerline. The first column is rendered using the ray model; the second, third and fourth columns are rendered using our wave optics model with 100 μm, 10 μm, and 1 μm radius respectively. In the large scale limit, the wave result (b) and the ray result (a) are very similar, except in the forward scattering setting the wave result shows a stronger forward scattering peak. However, as the size of the fibers decreases, we observe more colors along with broadening and smoothing of the highlight that are due to diffraction and interference effects, which cannot be predicted by the ray model. The last row shows ϕ_i vs. ϕ_r plots of the azimuthal scattering function for $\theta_i = 0$. The $1\mu m$ plot shows strong colors, which manifest themselves in the renders (d).

shadowing, and is often greater. That is, the ray theory commonly underestimates the total magnitude of the change caused by the presence of the fiber; or more informally, a fiber can scatter or absorb more light than is geometrically incident upon it.

This creates major energy conservation problems if the wave scattering results are used directly in a path tracer. The difference in total extinction between the two theories can be summarized by the *extinction cross section*, which is the fiber width required to shadow as much power as is extinguished under the wave model. The extinction cross section is a function of wavelength and incident direction in both θ and ϕ, unlike the geometric cross section, which depends only on incident ϕ. We propose to account for this difference by using the extinction cross section for fibers in the renderer instead of the original geometric cross section, as detailed in Section 5.1.

In addition to the energy conservation issue, wave-based scattering has no notion of discrete reflection and transmission events, so it cannot be separated into different modes by counting interactions. Thus we represent the wave-based azimuthal scattering function as a single mode and multiply it with a single longitudinal function, which currently prevents modeling the asymmetries due to cuticle scales in hair and fur.

4 2.5D WAVE SIMULATOR

The physical setting for our scattering simulation is the same as in previous ray-based fiber scattering models: we illuminate a straight dielectric fiber of constant cross-section with a collimated beam
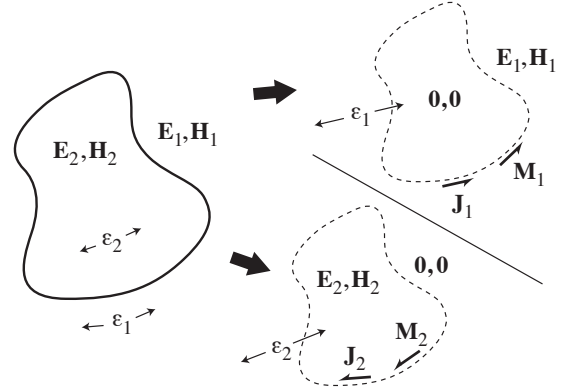

Fig. 5. Separation of interior and exterior fields via surface equivalence. The original problem (left) has fields both interior and exterior to the fiber with a change in material properties at the surface. We denote the exterior and interior regions as region 1 and 2 respectively. The original problem is transformed into a pair of problems (right), each in a homogeneous medium, with surface currents generating the field on one side and zero on the other side.

and predict the far-field distribution of scattered light. As with previous methods for computing the azimuthal pattern [Marschner et al. 2003], the translational symmetry of the problem removes one dimension (θ_r) from consideration, and this enables the 3D electromagnetic fields to be determined by a 2D calculation involving the cross-sectional shape of the fiber, an approach we refer to as 2.5D.

The rest of this section sketches our approach to formulating the scattering problem as a set of integral equations over the 1D boundary of the fiber's 2D cross section, numerically solving them using BEM, and interpreting the solution as a scattering function suitable for rendering. The general approach of using BEM to solve scattering problems is fairly standard in CEM, though this particular formulation is specialized to the problem of dielectric fibers. For a more complete treatment of the topic of electromagnetic wave scattering from objects, see Poggio and Miller [1970], Wu and Tsai [1977], and Huddleston et al. [1986].

4.1 Problem setup

The boundary of the fiber is the extrusion of a curve Γ in the x-y plane along the z axis. This surface divides space into exterior and interior regions, denoted 1 and 2 respectively, with different material properties (ϵ_1, μ_1) and (ϵ_2, μ_2) as in Figure 5 (left). For a dielectric fiber with complex refractive index $n + j\kappa$ surrounded by free space, $\epsilon_1 = \epsilon_0$, $\epsilon_2 = (n + j\kappa)^2\epsilon_0$, and $\mu_1 = \mu_2 = \mu_0$, where ϵ_0 and μ_0 are the permittivity and permeability of free space.

The fiber is illuminated by a plane wave propagating in direction $-\omega_i{}^1$. The incident electric and magnetic fields (i.e. fields in the

---

[1]Using linearity, other kinds of illumination can be handled by first expressing them as sums of plane waves.
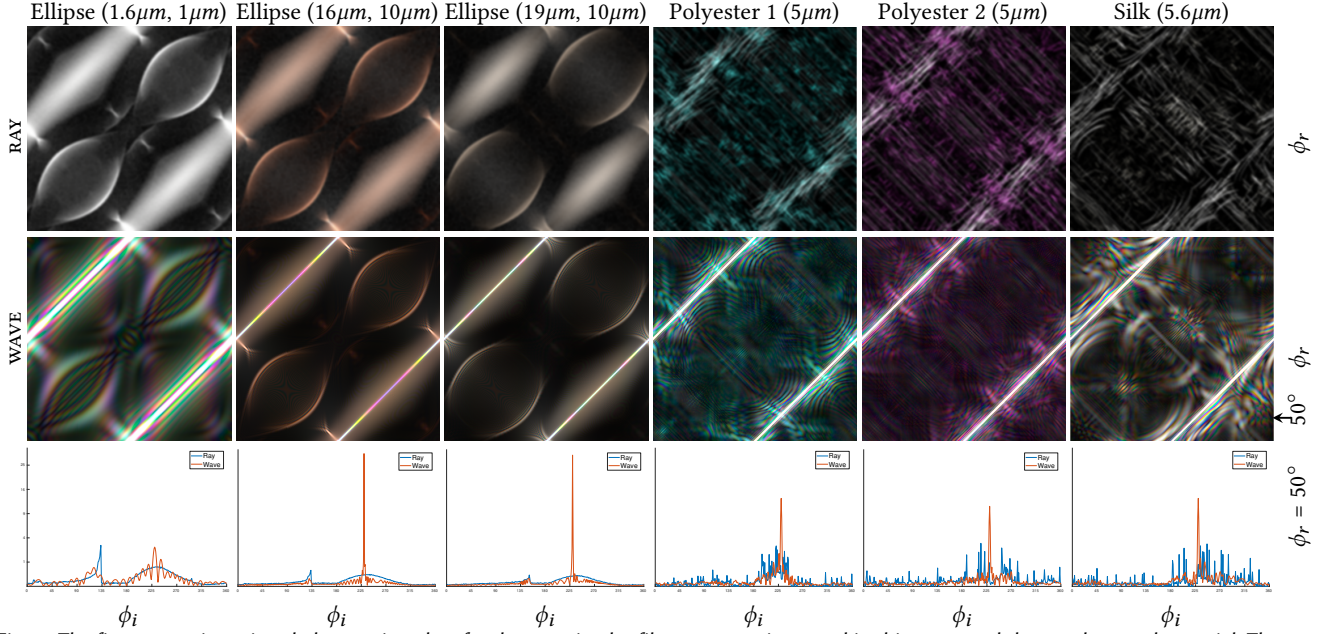
Fig. 6. The figure contains azimuthal scattering plots for the non-circular fiber cross sections used in this paper and the supplemental material. The top two rows show ϕ_i vs. ϕ_r plots at $\theta_i = 0$, with x-axis representing ϕ_i and y-axis representing ϕ_r. We integrated the scattering functions over wavelength to obtain the RGB representations in these colored plots. Our wave results (second row) contain rainbow colors and other features not present in the ray results (top row). The ray-based scattering functions for non-elliptical fibers are obtained by tracing rays through the cross sections (represented as line segments with linearly interpolated normal vectors). Compared to the ray-based distributions, the wave simulation produces much smoother distributions on the non-elliptical cross sections. In the bottom row, we plot 1D slices from the upper plots, specifically the square root of the scattering distribution at $\lambda = 400$nm and $\phi_r = 50°$.

absence of the fiber) are

$$\mathbf{E}_i(\mathbf{r}) = \mathbf{E}_i(0)\, e^{j\mathbf{k}\cdot\mathbf{r}}$$
$$\mathbf{H}_i(\mathbf{r}) = \mathbf{H}_i(0)\, e^{j\mathbf{k}\cdot\mathbf{r}} \tag{4}$$
$$\mathbf{H}_i(0) = -\frac{\mathbf{k}\times\mathbf{E}_i(0)}{\omega\mu_0}$$

where $\mathbf{E}_i(0)$ and $\mathbf{H}_i(0)$ define the wave's intensity and polarization, and the wavevector is $\mathbf{k} = k\omega_i$. The wavenumber is $k = \frac{2\pi}{\lambda}$ for light of wavelength λ and angular frequency $\omega = 2\pi/(\lambda\sqrt{\epsilon_0\mu_0})$. Here and in what follows, a time dependence $e^{j\omega t}$ is assumed and suppressed.

The presence of the fiber alters the fields and we call the resulting fields the *total fields* $\mathbf{E}_t, \mathbf{H}_t$. In the following subsections we will solve for the total fields by expressing them as sums of simpler fields $\mathbf{E}_1, \mathbf{H}_1$, which are zero in the interior of the fiber, and $\mathbf{E}_2, \mathbf{H}_2$, which are zero in the exterior. We further subdivide the exterior total fields into the incident fields and the *scattered fields* $\mathbf{E}_s, \mathbf{H}_s$ such that

$$\mathbf{E}_t = \mathbf{E}_1 + \mathbf{E}_2; \quad \mathbf{H}_t = \mathbf{H}_1 + \mathbf{H}_2 \tag{5}$$
$$\mathbf{E}_1 = \mathbf{E}_i + \mathbf{E}_s; \quad \mathbf{H}_1 = \mathbf{H}_i + \mathbf{H}_s \tag{6}$$

The scattered fields propagate outward from the fiber and will be the key to computing the BCSDF for rendering.

The fields obey the time-harmonic Maxwell's equations relating corresponding currents and fields

$$\nabla \times \mathbf{E} = -\mathbf{M} - j\omega\mu\mathbf{H}$$
$$\nabla \times \mathbf{H} = \mathbf{J} + j\omega\epsilon\mathbf{E}. \tag{7}$$

Here $\mathbf{J}$ and $\mathbf{M}$ are time-harmonic electric and magnetic current densities.[2]

4.2 Splitting the problem via surface equivalence

The surface equivalence principle [Love 1901; Schelkunoff 1936] states that fields $\mathbf{E}, \mathbf{H}$ that exist in a source-free region can be generated by surface currents $\mathbf{J}, \mathbf{M}$ residing on the region's boundary. This equivalence lets us transform our scattering problem into a pair of problems concerning unbounded homogeneous media, which are amenable to solution using Green's functions (Figure 5).

The surface equivalence principle implies that the fields $\mathbf{E}_s, \mathbf{H}_s$ (i.e. the source-free part of the fields in region 1) can be generated by surface currents $\mathbf{J}_1, \mathbf{M}_1$ residing on the boundary and radiating in unbounded free space. Likewise, $\mathbf{E}_2, \mathbf{H}_2$ can be generated by surface currents $\mathbf{J}_2, \mathbf{M}_2$ residing on the boundary and radiating in an unbounded medium consisting of fiber material. The fields $\mathbf{E}_1, \mathbf{H}_1$ can be made to vanish in region 2, and the fields $\mathbf{E}_2, \mathbf{H}_2$ can be set to zero in region 1, by requiring that

$$\mathbf{M}_1 = -\hat{\mathbf{n}}_1 \times \mathbf{E}_1, \quad \mathbf{J}_1 = \hat{\mathbf{n}}_1 \times \mathbf{H}_1$$
$$\mathbf{M}_2 = -\hat{\mathbf{n}}_2 \times \mathbf{E}_2, \quad \mathbf{J}_2 = \hat{\mathbf{n}}_2 \times \mathbf{H}_2 \tag{8}$$

where $\hat{\mathbf{n}}_1 = \hat{\mathbf{n}}$ and $\hat{\mathbf{n}}_2 = -\hat{\mathbf{n}}_1$ are surface normal vectors pointing towards region 1 and 2 respectively.

_____
[2]Although magnetic currents do not really exist, it is mathematically useful to include them in the formulation. In our case these will be fictitious currents introduced on the fiber boundary to divide our problem into two simpler homogeneous domains.

At a dielectric interface, the tangential components of the total electric and magnetic fields must be continuous such that

$$\hat{\mathbf{n}} \times \mathbf{E}_1 = \hat{\mathbf{n}} \times \mathbf{E}_2; \quad \hat{\mathbf{n}} \times \mathbf{H}_1 = \hat{\mathbf{n}} \times \mathbf{H}_2. \tag{9}$$

We can enforce these interface continuity constraints by requiring

$$\mathbf{J} = \mathbf{J}_1 = -\mathbf{J}_2; \quad \mathbf{M} = \mathbf{M}_1 = -\mathbf{M}_2. \tag{10}$$

In regions of space where ϵ and μ are constant, Maxwell's equations reduce to the Helmholtz equations [Harrington and Fields 1961]

$$\nabla^2 \mathbf{E} + k^2 \mathbf{E} = j\omega\mu \mathbf{J} - \frac{1}{j\omega\epsilon} \nabla(\nabla \cdot \mathbf{J}) + \nabla \times \mathbf{M}$$
$$\nabla^2 \mathbf{H} + k^2 \mathbf{H} = j\omega\epsilon \mathbf{M} - \frac{1}{j\omega\mu} \nabla(\nabla \cdot \mathbf{M}) - \nabla \times \mathbf{J} \tag{11}$$

which we can use to compute the fields generated by a set of currents. In particular from $\mathbf{J}_1$ and $\mathbf{M}_1$ we can compute the scattered fields $\mathbf{E}_s, \mathbf{H}_s$ and from $\mathbf{J}_2$ and $\mathbf{M}_2$ we can compute the fields $\mathbf{E}_2, \mathbf{H}_2$ (using the material parameters for regions 1 and 2 respectively). Therefore we use the currents to parameterize the fields in solving for them. This leads to the source field relations in the following section, which further enable the boundary integral formulation of the scattering problem.

4.3 Source field relations in 2.5D

In this section we develop a formal solution to (11) in a homogeneous medium, specialized to fibers with translational symmetry along the z axis. There is no need to compute the dependence of $\mathbf{J}, \mathbf{M}$, or any other quantities in the problem in the z direction, because the problem symmetry determines it. This will result in equations that describe the fields in 3D space using only currents defined on the 1D curve Γ. It's important to recognize that these currents and fields, while they are defined over a 2D domain, are still 3D quantities, and the vectors have components both in the x-y plane and in the z direction.

We adopt the coordinate system shown in Figure 2, and represent the 3D and 2D coordinates using $\mathbf{r} = x\hat{\mathbf{x}} + y\hat{\mathbf{y}} + z\hat{\mathbf{z}}$ and $\boldsymbol{\rho} = x\hat{\mathbf{x}} + y\hat{\mathbf{y}}$.

The incident field can be expressed as

$$\mathbf{E}_i = \mathbf{E}_0 e^{j\mathbf{k}_\rho \cdot \boldsymbol{\rho}} e^{jk_z z}, \quad \mathbf{H}_i = \mathbf{H}_0 e^{j\mathbf{k}_\rho \cdot \boldsymbol{\rho}} e^{jk_z z} \tag{12}$$

where $\mathbf{k} = \mathbf{k}_\rho + k_z\hat{\mathbf{z}}$ and $k_\rho = |\mathbf{k}_\rho|$. Since the z dependence of this source field is a complex exponential, a translation in z corresponds to multiplying the field by a global scalar phase factor. Since (11) is a linear PDE, scaling the source will scale all the quantities in the problem by the same factor; hence all the fields and currents inherit the same z dependence as $\mathbf{E}_i, \mathbf{H}_i$:

$$\mathbf{E}(\mathbf{r}) = \mathbf{E}(\boldsymbol{\rho})e^{jk_z z}, \quad \mathbf{H}(\mathbf{r}) = \mathbf{H}(\boldsymbol{\rho})e^{jk_z z},$$
$$\mathbf{J}(\mathbf{r}) = \mathbf{J}(\boldsymbol{\rho})e^{jk_z z}, \quad \mathbf{M}(\mathbf{r}) = \mathbf{M}(\boldsymbol{\rho})e^{jk_z z}. \tag{13}$$

Applying the z dependence described above to the Helmholtz equation (11), we obtain the 2.5D wave equations. With the corresponding Green's function, we can write out the *2.5D source field relations* as convolutions of the electric and magnetic sources on the right hand side of (11) with the Green's function. The result has a similar

form for $\mathbf{E}$ and $\mathbf{H}$ and can be written in terms of integral linear operators $\mathcal{L}$ and $\mathcal{K}$ as:

$$\mathbf{E}(\boldsymbol{\rho}) = -j\omega\mu\mathcal{L}\mathbf{J}(\boldsymbol{\rho}) - \mathcal{K}\mathbf{M}(\boldsymbol{\rho}), \tag{14}$$

$$\mathbf{H}(\boldsymbol{\rho}) = -j\omega\epsilon\mathcal{L}\mathbf{M}(\boldsymbol{\rho}) + \mathcal{K}\mathbf{J}(\boldsymbol{\rho}). \tag{15}$$

where

$$(\mathcal{L}\mathbf{X})(\boldsymbol{\rho}) = \left[1 + \frac{1}{k^2}\nabla\nabla\cdot\right] \int_\Gamma e^{jk_z z} G\left(\boldsymbol{\rho}, \boldsymbol{\rho}'\right) \mathbf{X}(\boldsymbol{\rho}')d\boldsymbol{\rho}'\Big|_{z=0}, \tag{16}$$

$$(\mathcal{K}\mathbf{X})(\boldsymbol{\rho}) = \nabla \times \int_\Gamma e^{jk_z z} G\left(\boldsymbol{\rho}, \boldsymbol{\rho}'\right) \mathbf{X}(\boldsymbol{\rho}')d\boldsymbol{\rho}'\Big|_{z=0}. \tag{17}$$

In (16) and (17), $\mathcal{L}$ is a linear operator operating on electric (magnetic) currents to produce contribution to the electric (magnetic) fields; $\mathcal{K}$ is a linear operator operating on magnetic (electric) currents to produce contribution to the electric (magnetic) fields. $G(\boldsymbol{\rho}, \boldsymbol{\rho}')$ is the Green's function for the 2D Helmholtz equation and represents the field at $\boldsymbol{\rho}$ produced by a line source at $\boldsymbol{\rho}'$; it satisfies

$$\nabla^2 G\left(\boldsymbol{\rho}, \boldsymbol{\rho}'\right) + k_\rho^2 G\left(\boldsymbol{\rho}, \boldsymbol{\rho}'\right) = -\delta\left(\boldsymbol{\rho}, \boldsymbol{\rho}'\right). \tag{18}$$

This equation's solution is

$$G(\boldsymbol{\rho}, \boldsymbol{\rho}') = \frac{1}{4j} H_0^{(2)}(k_\rho|\boldsymbol{\rho} - \boldsymbol{\rho}'|) \tag{19}$$

where $H_0^{(2)}$ is the zeroth order Hankel function of the second kind.

The 2.5D source field relations (Equations (14) and (15)) are formal solutions to Maxwell's equations, in that they express the fields directly as integral operators applied to the current densities. The source field relation equations apply separately to the interior and exterior problems: they relate $\mathbf{J}_1, \mathbf{M}_1$ to $\mathbf{E}_s, \mathbf{H}_s$ using the k, ϵ and μ for region 1; and likewise they relate $\mathbf{J}_2, \mathbf{M}_2$ to $\mathbf{E}_2, \mathbf{H}_2$ using the parameters for region 2. And once $\mathbf{J}_1$ and $\mathbf{M}_1$ are known, they can be used to compute the scattered fields in the exterior. More derivation details can be found in the supplemental document.

4.4 Solving for the currents

We now have the ingredients needed to assemble an integral equation for $\mathbf{J}, \mathbf{M}$ that we can discretize and solve. Combining the boundary current constraints in Equations (8), (10) with source field relations, we can eliminate the fields, resulting in integral equations for $\mathbf{J}$ and $\mathbf{M}$, given the known incident fields, known as the electric field integral equations (EFIE):

$$\mathbf{M}(\boldsymbol{\rho}) + \hat{\mathbf{n}}_1(\boldsymbol{\rho}) \times \left[-j\omega\mu_1\left(\mathcal{L}_1\mathbf{J}\right)(\boldsymbol{\rho}) - (\mathcal{K}_1\mathbf{M})(\boldsymbol{\rho})\right] = -\hat{\mathbf{n}}_1(\boldsymbol{\rho}) \times \mathbf{E}_i(\boldsymbol{\rho})$$
$$\mathbf{M}(\boldsymbol{\rho}) + \hat{\mathbf{n}}_2(\boldsymbol{\rho}) \times \left[-j\omega\mu_2\left(\mathcal{L}_2\mathbf{J}\right)(\boldsymbol{\rho}) - (\mathcal{K}_2\mathbf{M})(\boldsymbol{\rho})\right] = 0, \tag{20}$$

and the magnetic field integral equations (MFIE):

$$\mathbf{J}(\boldsymbol{\rho}) - \hat{\mathbf{n}}_1(\boldsymbol{\rho}) \times \left[-j\omega\epsilon_1\left(\mathcal{L}_1\mathbf{M}\right)(\boldsymbol{\rho}) + (\mathcal{K}_1\mathbf{J})(\boldsymbol{\rho})\right] = \hat{\mathbf{n}}_1(\boldsymbol{\rho}) \times \mathbf{H}_i(\boldsymbol{\rho})$$
$$\mathbf{J}(\boldsymbol{\rho}) - \hat{\mathbf{n}}_2(\boldsymbol{\rho}) \times \left[-j\omega\epsilon_2\left(\mathcal{L}_2\mathbf{M}\right)(\boldsymbol{\rho}) + (\mathcal{K}_2\mathbf{J})(\boldsymbol{\rho})\right] = 0 \tag{21}$$

where $\mathcal{L}_1$ (resp. $\mathcal{L}_2$) is the $\mathcal{L}$ operator defined using the wavenumber for region 1 (resp. 2), and similarly for $\mathcal{K}_1$ and $\mathcal{K}_2$.

Equations (20) and (21) constitute four equations in two unknowns. Here, we combine them so as to ensure their solution
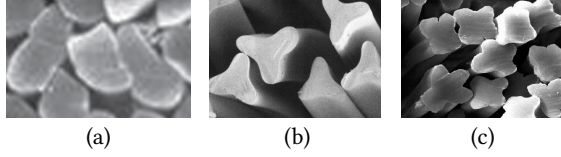
Fig. 7. Besides different sizes of circular fibers and elliptical fibers, our wave-based BCSDF is also able to model light scattering on more irregular cross sections. The above are scanning electron microscope (SEM) images of three irregular cross-sectional shapes that we exemplify in this work. a) is silk cross section, often in polygonal-like shapes. b) and c) are two types of polyester cross sections. Images (a), (b) and (c) are from [Babu 2018], [Lee et al. 2003] and [Varshney et al. 2011] respectively.

is unique. The specific combination strategy adopted here is the PM-CHWT approach [Poggio and Miller 1970], resulting in the smaller system

$$\hat{\mathbf{n}} \times [-j\omega(\mu_1 \mathcal{L}_1 + \mu_2 \mathcal{L}_2) \mathbf{J} - (\mathcal{K}_1 + \mathcal{K}_2) \mathbf{M}] = -\hat{\mathbf{n}} \times \mathbf{E}_i$$
$$-\hat{\mathbf{n}} \times [-j\omega(\epsilon_1 \mathcal{L}_1 + \epsilon_2 \mathcal{L}_2) \mathbf{M} + (\mathcal{K}_1 + \mathcal{K}_2) \mathbf{J}] = \hat{\mathbf{n}} \times \mathbf{H}_i. \tag{22}$$

Discretization and linear system. We solve for the unknown currents by applying a Galerkin-type method to convert Equation (22) into a linear system [Rylander et al. 2012]. First, we discretize the fiber cross-section boundary Γ into N line segments and represent both the electric and magnetic surface currents using the same set of $2N$ linear basis functions $\mathbf{f}$:

$$\mathbf{J}(\boldsymbol{\rho}) \approx \sum_{i=1}^{2N} (I_J)_i \mathbf{f}_i(\boldsymbol{\rho}), \quad \mathbf{M}(\boldsymbol{\rho}) \approx \sum_{i=1}^{2N} (I_M)_i \mathbf{f}_i(\boldsymbol{\rho}) \tag{23}$$

Each basis function is supported over two adjacent elements. The first N of the $2N$ basis functions represent z-directed currents, while the other N represent currents that flow on the fiber surface orthogonal to z.

Substituting the approximation (23) into the system (22) and testing the resulting equations using the same basis $\mathbf{f}$ leads to a matrix equation

$$\begin{bmatrix} Z_{ME} & Z_{JE} \\ Z_{MH} & Z_{JH} \end{bmatrix} \begin{bmatrix} I_M \\ I_J \end{bmatrix} = \begin{bmatrix} V_E \\ V_H \end{bmatrix}. \tag{24}$$

where the submatrices are formed from inner products of testing functions with the components of (22)

$$\begin{aligned}
(Z_{ME})_{ik} &= -\langle \mathbf{f}_i, \hat{\mathbf{n}} \times ((\mathcal{K}_1 + \mathcal{K}_2) \mathbf{f}_k) \rangle \\
(Z_{JE})_{ik} &= -j\omega \langle \mathbf{f}_i, \hat{\mathbf{n}} \times ((\mu_1 \mathcal{L}_1 + \mu_2 \mathcal{L}_2) \mathbf{f}_k) \rangle \\
(Z_{MH})_{ik} &= j\omega \langle \mathbf{f}_i, \hat{\mathbf{n}} \times ((\epsilon_1 \mathcal{L}_1 + \epsilon_2 \mathcal{L}_2) \mathbf{f}_k) \rangle \\
(Z_{JH})_{ik} &= -\langle \mathbf{f}_i, \hat{\mathbf{n}} \times ((\mathcal{K}_1 + \mathcal{K}_2) \mathbf{f}_k) \rangle \\
(V_E)_i &= \langle \mathbf{f}_i, -\hat{\mathbf{n}} \times \mathbf{E}_i \rangle \\
(V_H)_i &= \langle \mathbf{f}_i, \hat{\mathbf{n}} \times \mathbf{H}_i \rangle.
\end{aligned} \tag{25}$$

Here we define the inner product between a pair of vector functions $\mathbf{a}$ and $\mathbf{b}$ as

$$\langle \mathbf{a}, \mathbf{b} \rangle = \int_{\Gamma} \mathbf{a}(s) \cdot \mathbf{b}(s) \, ds \tag{26}$$

This block matrix system has a total dimension $4N \times 4N$. Z_{ME} represents the block where we express $\mathbf{M}$ in EFIE (E) using the basis functions $\mathbf{f}$ and apply the same set of basis functions as testing functions. The other blocks are named analogously. V_E and V_H are

the test integrals on the incident electric field and magnetic field. Finally, we solve for the coefficients I_M and I_J, and we obtain from (23) the surface currents $\mathbf{J}(\boldsymbol{\rho})$ and $\mathbf{M}(\boldsymbol{\rho})$, which are the equivalent surface sources that define the solution to our scattering problem.

4.5 Computing far-field quantities

Having computed the surface currents, we can use the source field relations (Equations (14) and (15)) to compute the scattered electric field ($\mathbf{E}_s$) and the scattered magnetic field ($\mathbf{H}_s$) on an observing circle with radius R. The quantity of interest is the azimuthal scattering function, which describes the distribution of scattered light within the specular cone. In electromagnetics, the Poynting vector represents the energy transfer per unit area per unit time. We are interested in the time-averaged Poynting vector, which can be calculated as the real part of the cross product of the electric field and the conjugate of the magnetic field:

$$\langle \mathbf{S} \rangle = \tfrac{1}{2} \mathrm{Re}(\mathbf{E} \times \mathbf{H}^*). \tag{27}$$

The time-averaged Poynting vector is equivalent to vector irradiance in radiometry and it provides a way to compute the azimuthal distribution from the scattered field.

The quantities we can compute from the simulation include the angular distribution of scattered intensity per unit length and the absorbed power per unit length.

Scattered intensity. We conduct scattered far-field calculations using asymptotic forms of the 2D Green's function [Gibson 2014]. Then scattered intensity per unit length can be calculated as

$$I_s(\theta_i, \phi_i, \phi_r, \lambda) = \tfrac{1}{2} \mathrm{Re}(\mathbf{E}_{S_{\mathrm{far}}} \times \mathbf{H}^*_{S_{\mathrm{far}}}) \cdot \boldsymbol{\rho}(\phi_r), \tag{28}$$

where $\boldsymbol{\rho}(\phi_r)$ is the vector in the $x - y$ plane, pointing away from the origin and forming an angle of ϕ_r with the x-axis, with $|\boldsymbol{\rho}(\phi_r)|$ much greater than the fiber radius. The total scattered power per unit length, W_s, can be obtained by integrating $I_s(\phi_r)$.

Absorption. Absorbed power per unit length can be calculated by integrating the normal component of the total field's Poynting vector over the boundary, as the net flow at the boundary is the absorption:

$$\begin{aligned}
W_a &= \int_{\Gamma} \frac{1}{2} \mathrm{Re}(\mathbf{E}_1 \times \mathbf{H}^*_1) \cdot \hat{\mathbf{n}}_1(s) \, ds \\
&= \int_{\Gamma} \frac{1}{2} \mathrm{Re}(\mathbf{J}^*_1 \times \mathbf{M}_1) \cdot \hat{\mathbf{n}}_1(s) \, ds.
\end{aligned} \tag{29}$$

The second equation is derived by applying Equation (8).

5 WAVE OPTICS FIBER BCSDF

With the tools of the previous sections, we have the ability to solve wave scattering problems for arbitrary cylinders under arbitrary incident fields, either by using the Mie solution [Bohren and Huffman 2008] for circular cylinders or the BEM computation for arbitrary cross sections. For a particular fiber, we run a set of simulations using plane wave incident fields with different directions and wavelengths, each resulting in a scattered field. In this section we discuss how to use these solutions in a path tracer by defining a BCSDF that, when applied to an isolated curve primitive, matches the far-field behavior of the wave simulation.

As we discussed in Section 3.2, scattering of an incident field by a fiber produces a far-field intensity distribution that is the sum of three components: the incident beam; the scattered intensity; and the extinction, a generally negative contribution from interference between the scattered and incident fields. Energy balance requires matching the integrals of these three distributions in the ray tracer, which we do by matching the diameter of the fiber to the total extinction, then normalizing the scattered distribution to the total extinction to define the BCSDF.

5.1 Fiber cross section

From the scattered field for a particular incident direction and wavelength, we compute the scattered power per unit length, $W_s \geq 0$, and the absorbed power per unit length, $W_a \leq 0$ (Section 4.5); then $W_x = W_a - W_s \leq 0$ is the extinction power per unit length. Dividing by the projected irradiance of the incident beam gives the width of fiber that geometrically receives power per unit length equal to $|W_x|$:

$$C_x = \frac{|W_x|}{\langle \mathbf{S}_i \rangle \cdot \omega_i \cos \theta_i} = \frac{|W_a - W_s|}{\frac{1}{2} \mathrm{Re}(\mathbf{E}_i \times \mathbf{H}_i^*) \cdot \omega_i \cos \theta_i} \tag{30}$$

We call the width C_x the extinction cross section.

In order to obtain consistent results between the renderer and the wave simulation, the width of the fiber seen by rays in the scene needs to match C_x, even though it is different from the geometric cross section C_g. If this requirement is overlooked, either fibers will scatter the wrong intensity, or the system will fail to conserve energy, causing recursive path tracing results that are too bright in the common case where $C_x > C_g$ (Figure 8 (b)).

A similar issue arises in simulating non-circular fibers, which even in the ray model present different widths to incident light from different directions, and in both cases we call the required width the *effective cross section* $C_e(\omega_i, \lambda)$: in the ray case, $C_e = C_g(\phi_i)$, and in the wave case, $C_e = C_x(\theta_i, \phi_i, \lambda)$. Our renderer supports only a single diameter at any point along a curve primitive, but a simple extension to the ray intersection algorithm achieves an effective width smaller than the intersection primitive by rejecting ray hits when the ray is too far from the centerline (see Section 6).

5.2 BCSDF

For rays that hit the fiber, the BCSDF describes the distribution of scattered light over the sphere of outgoing directions. This is simply the far-field scattered intensity per unit length normalized to the extinction power per unit length:

$$N_{\mathrm{wave}}(\theta_i, \phi_i, \phi_r, \lambda) = \frac{I_s(\theta_i, \phi_i, \phi_r, \lambda)}{|W_x(\theta_i, \phi_i, \lambda)|} \tag{31}$$

N_{wave} is the azimuthal function used to build the BCSDF as described in (2):

$$S(\theta_i, \theta_r, \phi_i, \phi_r, \lambda) = M_0(\theta_i, \theta_r) N_{\mathrm{wave}}(\theta_i, \phi_i, \phi_r, \lambda),$$

where the longitudinal function M_0 is evaluated following d'Eon et al. [2011].

5.2.1 Evaluation. For each type of fiber, we precompute N_{wave} as a function of $(\theta_i, \phi_i, \phi_r, \lambda)$ and store it in tables; at rendering time, we interpolate the tables to evaluate the BCSDF. Our renderer uses

(a) Ray, conventional, conserving energy

(b) Wave, naive, excessive energy

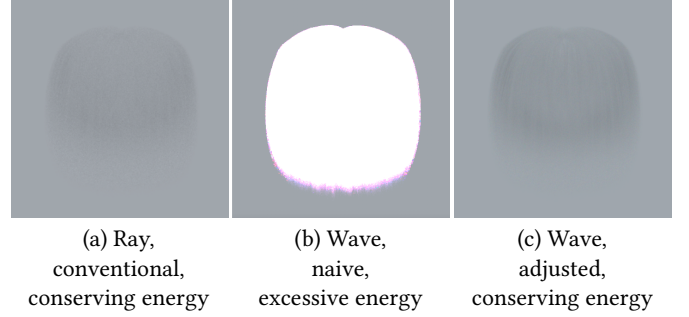(c) Wave, adjusted, conserving energy

Fig. 8. A furnace test comparison on a head of white hair in a constant environment. The conventional ray-based BCSDF (a) and our wave-based BCSDF (c) conserve energy and will eventually disappear in the environment as we keep increasing the number of bounces. The naive wave-based BCSDF without the adjusted cross-section has excessive energy because the actual incident energy in the wave sense is more than what the ray tracer collects. We describe the effective cross section adjustment in subsection 5.1.

discretized wavelengths, so the azimuthal function is computed using trilinear interpolation on the θ_i, ϕ_i and ϕ_r dimensions.

For ϕ_i and ϕ_r, we use the band-limitedness of the fields [Piestun and Miller 1999] to compute a sufficient sampling rate based on the fiber size. For the θ_i and λ dimensions, we increase the sampling rate until there is no visible change in a rendering test. The required sampling rates grow as the size of the fiber increases relative to the wavelength because the distributions contain higher frequency features. However, due to the averaging over wavelength and incident angles that happen in rendering, in practice we find that we can bound the sampling rates and still faithfully reproduce the appearance. For a cylinder of arbitrary cross section, we store its azimuthal function using no more than 50 wavelength samples, 100 θ_i samples, 360 ϕ_i samples and 360 ϕ_r samples. For cross sections that possess symmetry, we can decrease ϕ_i sample counts accordingly. For large fibers, we first densely sample the four dimensions to prevent aliasing, then average the BCSDFs down to the above size to save memory. For circular, elliptical and arbitrary fibers, it takes 7.2MB, 0.7GB and 2.6GB respectively to store an azimuthal function (using 32-bit floats).

5.2.2 Sampling. In a Monte Carlo renderer we also need to be able to efficiently sample the BCSDF. In our tabulated setting this is easy to do by normalizing N_{wave} separately per wavelength, θ_i and ϕ_i, resulting in almost perfect importance sampling for a fixed wavelength.

Because the BCSDF can vary dramatically with wavelength, and because the fiber width depends on wavelength, we opt for rendering with a single wavelength per path. This eliminates difficulties with rays that hit at some wavelengths and miss at others, and also avoids the need to find a compromise PDF that achieves good importance sampling across all wavelengths simultaneously.

Figure 8 (c) demonstrates that these computations successfully achieve energy balance in the path tracer. We further validate the match between the wave simulation and its representation in the path tracer in Section 7.2.
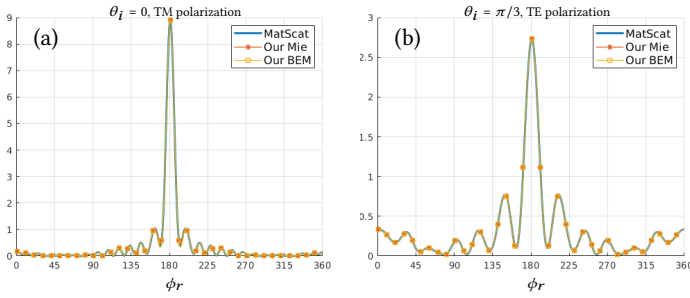
Fig. 9. We validate our Mie and BEM solver against MatScat[Schäfer 2020; Schäfer et al. 2012; Schäfer 2011] on circular cylinder scattering. This comparison shows the scattering intensity distribution for a $1\mu m$ radius fiber for wavelength 400nm. a) shows TM polarization for normal incidence ($\theta_i = 0$); b) shows TE polarization for $\theta_i = \pi/3$. Our Mie implementation matches MatScat perfectly and the error of the BEM solver is within 1%.
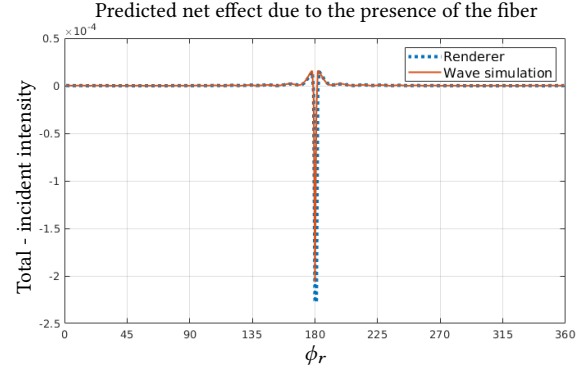

Fig. 10. We computed the net effect due to the presence of the fiber both in wave simulation and in the renderer. This net effect is the difference between the total intensity and the incident intensity. It is computed as a function of ϕ_r for a particular fiber at a single wavelength and incident direction. This plot shows that the integration of the wave azimuthal function into the renderer reproduces the net effect with good accuracy.

6 IMPLEMENTATION

Wave simulation and acceleration. We implemented our wave optics fiber scattering simulation in C++. For scattering from infinitely long circular cylinders, the analytic Mie solution [Bohren and Huffman 2008] to Maxwell's equations is available. This method is much less expensive than the Boundary Element Method as it does not involve assembling and solving a large matrix. However, it is limited to circular cross sections. For cylinders with arbitrary cross-sectional shapes, we implemented our own BEM solver. For linear algebra computation, we used the Eigen library [Guennebaud et al. 2010] and for special function calculations we used the Complex_Bessel C++ interface [Dumont and Gagnon 2013] that calls the FORTRAN implementation of Amos [1986]. Several optimizations are important in this implementation. First, the Hankel function evaluations needed to evaluate the Green's function during matrix assembly are a bottleneck, so we precompute these functions with complex arguments and store them as tables. Also, once the cross section and material properties are fixed, we need to run simulations for many wavelengths, incident directions, and for two polarizations. This results in solving the linear system (24) repeatedly. However, as Z only depends on wavelength and θ_i, but not ϕ_i and polarization, we only need to assemble Z once and conduct one LU factorization for all ϕ_i and different polarizations. Besides accelerating the special function evaluation and the linear system solve, we also parallelize the simulations for different θ_i. These three levels of acceleration speed up the simulation by 3 orders of magnitude. Our code is available on the project page[3].

Ray traced BCSDF. To compare our wave-based BCSDF to a ray-based BCSDF for fibers with arbitrary cross sections, we also developed a 2D ray tracer that can compute the azimuthal scattering distribution of any cross-section shape. This 2D ray tracer constructs ellipses parametrically and constructs more irregular shapes using line segments with linearly interpolated normals. It computes the scattering distribution by binning the scattered rays.

Integrating tabluated BCSDF into a renderer. We integrated our precomputed wave-based and ray-based BCSDFs into PBRT [Pharr and Humphreys 2010] by introducing two new materials. In Section 5.1, we define the effective cross section C_e, which equals to the equivalent fiber width that light interacts with. In the ray case, C_e depends on ϕ_i for non-circular fibers; in the wave case, C_e depends on the incident direction and the wavelength. It is crucial to account for C_e to achieve energy balance but it is not practical to instantiate a new primitive when the incident direction or the wavelength changes. Therefore, we use a bounding circular cylinder with its diameter equal to the maximum[4] of C_e over incident directions and wavelengths as the intersection primitive. We apply an offset-limited intersection scheme to achieve an effective width. This scheme determines whether a ray hits the fiber by comparing the offset of the ray from the fiber centerline with C_e.

7 VALIDATION

We validated our implementation using three tests: comparing our Mie and BEM solutions to those from an existing Mie solver for the special case of a circular fiber; comparing the wave simulation and our path tracer implementation under matching illumination; and comparing our simulation result against a simple physical measurement.

7.1 Wave simulation

We compared our Mie implementation and BEM solver for circular fibers with an open-source Mie implementation, MatScat [Schäfer 2020; Schäfer et al. 2012; Schäfer 2011]. We tested various fiber sizes, incident θ_i angles, complex refractive indices, wavelengths and two polarizations, and found excellent agreement between all three solvers. Figure 9 shows azimuthal scattered intensity comparisons for two configurations. Our Mie implementation matches MatScat

---

[3]http://mandyxmq.github.io/research/wavefiber.html

[4]In the wave case, we clamp the maximum of C_e to at most 6 times the fiber's original geometric cross section to prevent any arbitrarily large values.
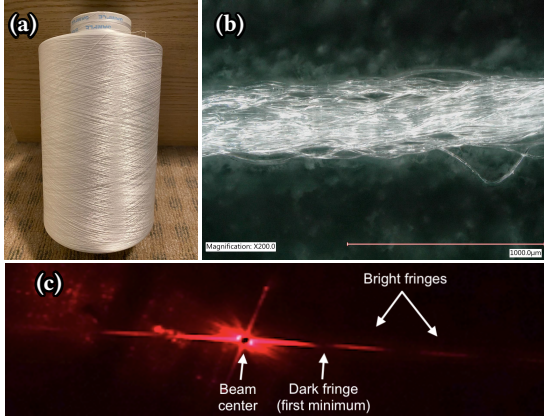
Fig. 11. We separated one fiber from the yarn sample shown in (a) and under 200x magnification in (b) and illuminated it with a red laser at normal incidence. We then observed its scattered light pattern on a diffuse paper target, with a hole at the beam's location. (c) is a photograph capturing the fiber scattering pattern when the target is 65cm away from the fiber. (Micrograph (b) courtesy of Manwen Li.)
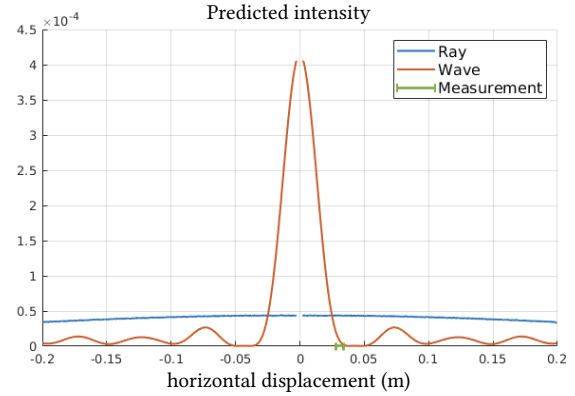

Fig. 12. This figure compares the ray and the wave predictions of a single fiber under laser beam scattering. We skip plotting the values near the forward direction to mimic the hole on the collecting paper in the measurement that lets the incident beam go through. The wave result predicts an oscillating pattern that is more consistent with what is observed in the experiment (Figure 11 (c)) than the monotonically decaying component predicted by the ray method. We use a horizontal error bar to mark the range of the measured first minima. The wave predicted and measured first minima do not exactly align because we used Babinet's principle for opaque objects to estimate the refractive fiber's size.

perfectly and the error of our BEM solver is less than 1% with 300 line segments.

7.2 Integration to the rendering system

We validated the integration of our wave optics azimuthal function into the renderer by comparing the net effect of the fiber on the far-field radiance distribution. For a particular fiber, wavelength and incident direction, the net effect can be computed as the total intensity minus the incident intensity as a function of ϕ_r.

In the wave case, we used a Gaussian beam to compute the net effect. Unlike a plane wave, a Gaussian beam is a non-singular incident distribution, so we can take a meaningful far-field limit and compute the total field intensity minus incident field intensity. It provides a way to evaluate the accuracy of integrating the wave BCSDF into the renderer. In addition, a Gaussian beam does not introduce actual simulation cost to our computation. One can post-process plane wave simulation results to produce beam solutions for any beam widths and offset values. In practice, we choose a Gaussian beam that is ten times wide as the fiber radius so that the incident field is mostly constant across the fiber.

In the renderer, we traced rays with density and angular distribution matching this Gaussian beam. For rays that intersect the effective cross section, we sampled scattered directions using the precomputed azimuthal function, otherwise the rays kept their initial direction. The resulting ray distribution corresponds to the total intensity distribution. The incident intensity is given by the initial ray directions. Figure 10 demonstrates that the net effect produced in the renderer is very close to the results of the wave simulation. The small differences near the forward direction are due to the fact that the geometric shadow and wave shadow are not quite the same shape.

7.3 Measurements

To demonstrate the presence of wave optics effects in real fiber scattering, we illuminated a single fiber with a laser beam and photographed the resulting scattering pattern. The scattering pattern has bright and dark fringes similar to those predicted by our wave-based model and which are absent from prior ray-based models.

We manually extracted individual polyester fibers from the yarn sample shown in Figure 11 (a) and (b). Next we illuminated a single fiber at normal incidence with a red laser and so that its scattered light falls onto a distant piece of paper. A small hole in the paper allows the remaining unscattered beam to pass through. We then estimated the location of the first minimum, or dark fringe, in the main scattering pattern as shown in Figure 11 (c). These scattering images also contain several fainter patterns with different alignments, and we speculate that these may be due to fiber imperfections, such as residual kinks or bends from having previously been twisted into a yarn. Nevertheless, the presence of fringes is a strong indicator of wave-optics effects.

We repeated this experiment for three fibers and three orientations for each fiber and found similar first minima in each, ranging from 2.8 to 3.4cm from the beam center. Babinet's principle [Born and Wolf 1999] states that the diffraction from an opaque object is identical to that of a hole of the same shape (except for the forward beam intensity). Using this principle, we can roughly estimate the size of any occluder from the location of the first minimum as:

$$D = \frac{\lambda L}{y}. \tag{32}$$

where D is the occluder width (or fiber diameter), $\lambda = 650$nm is the wavelength, $L = 65$cm is the distance to the paper, and y is the location of the first minimum. This gives an average estimated fiber

diameter of 13.8μm, which is close to our visual estimate of 13.1μm from the microscopy image in Figure 11 (b).

We also estimated the laser pointer's beam divergence and used it to compute wave and ray simulations of the fiber scattering to compare with the observed pattern. To make a fair comparison, the ray simulation used rays with density and angular distribution matching the estimated beam. Figure 12 compares these wave and ray predictions. The wave result shows an oscillating pattern that is similar to the observed diffraction fringes. The first fringe minimum prediction is close to our observed values of 2.8 to 3.4cm. The ray method, however, predicts a simple monotonic decrease away from the forward direction which does not match the observed scattering pattern. The small mismatch in the wave predicted minimum location is because we used Babinet's principle for opaque objects to roughly estimate the refractive fiber's size.

8 RESULTS

In this section, we demonstrate that our wave optics based fiber scattering model is able to handle fibers with different sizes, arbitrary cross section shapes and material properties by rendering different types of fibers in various environments. In addition, we compare our wave optics based fiber scattering model with the ray optics fiber scattering model and examine the similarities and differences of the two methods. We conduct the comparisons both by directly showing their azimuthal distributions (Figure 6) and by rendering fibers under different conditions. Also, we showcase an animal fur scene with textured fiber colors (Figure 16).

8.1 Strong color effects for thin fibers

A wave-based scattering function by nature is always wavelength dependent, even in the lossless fiber case. Our wave-based fiber scattering model is able to handle diffraction and interference effects that conventional ray models cannot. In Figure 4 and Figure 13 we show rendering comparisons of one layer of aligned fibers lit by a point source. We render both with the light source close to the camera and behind the fibers to observe backscattering and forward scattering effects respectively. In Figure 4, we show that the rendering from ray optics matches with that from wave optics pretty well at large geometric scale except that the wave optics results have a stronger forward scattering peak. There are substantial differences for small scale fibers. In particular, wave optics predicts rainbow colors that cannot be reproduced in the ray results. These colors can be observed in the ϕ_i vs. ϕ_r plots as well.

We render a spider web iridescence example in Figure 1. In this figure, we compare renderings produced using our wave-based method and a ray-based model (Figure 1(b) and (c)) to a photograph (Figure 1(a)). We are able to produce strong color effects due to diffraction and interference while the ray model cannot.

8.2 Forward scattering

Compared to the wave BCSDF predictions, the previous ray model has less energy in the forward scattering direction and this results in appearance differences, especially in the backlit setting. In Figure 14 we show one frame of the orbit renderings with a head of curly black hair under an area light and an environment light. The ray
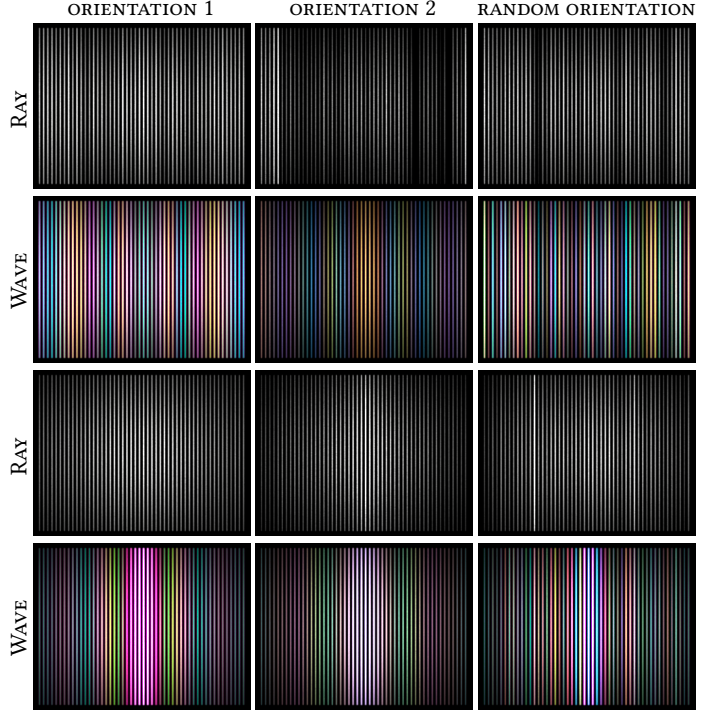
Fig. 13. We compare renders of 1 layer aligned fibers with an elliptical cross-section under a point light. In the top two rows, the light is close to the camera, showing backscattering effects. in the bottom two rows, the light is behind the layer of fibers, showing forward scattering effects. Row 1 and 3 are rendered using the ray-based BCSDF while row 2 and 4 are rendered using our wave-based BCSDF. In columns 1 and 2, we set the fibers to have two different constant orientation angles, while in the last column fibers are oriented randomly. The elliptical fibers' semi-major axis equals 1.6 μm and semi-minor axis equals to 1μm. We observe that the wave renders have strong color effects, which are not in the ray predictions. In additions, the distributions are also different and result in highlight differences between the ray results and the wave results.

result is lacking energy near the forward direction and results in a dimmer appearance on the edge of the hair model. Forward scattering appearance differences are also shown in Figure 4 and Figure 13. Strong forward scattering in cylindrical particles was also observed in paper fibers [Linder 2014].

8.3 Other appearance differences

We compare wave optics results and ray optics results in more complex settings. As more randomness is added (by averaging over light sources and multiple bounces), the color effects caused by diffraction and interference start to average out. However, we still observe appearance differences. In Figure 15 and Figure 16, the wave results produce smoother and softer highlights. In the wave render of Figure 16, individual fibers become less distinct and there is more overall translucency in the fur. In Figure 17, the wave and ray methods produce different shapes of highlight. We refer the reader to the supplemental webpage to better observe the differences.
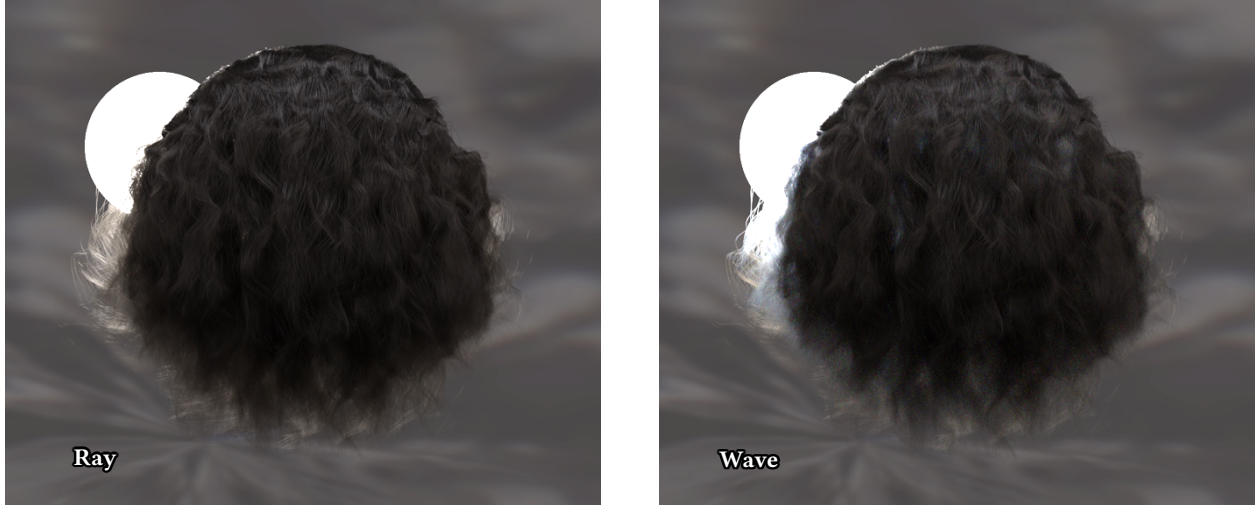
Fig. 14. This figure shows one frame of the orbit renderings where we have a head of elliptical curly black hair under an environment light and a rotating area light. The aspect ratio of these elliptical fibers is 1.9 and for the wave model, we set the ellipse semi-major and semi-minor axes to be $19\mu m$ and $10\mu m$. The wave result produces softer and brighter highlights on the edges of the model, which one can observe from backlit scenarios. The previous ray model misses energy near the forward scattering direction and this results in the backlit appearance not bright enough on the edge.
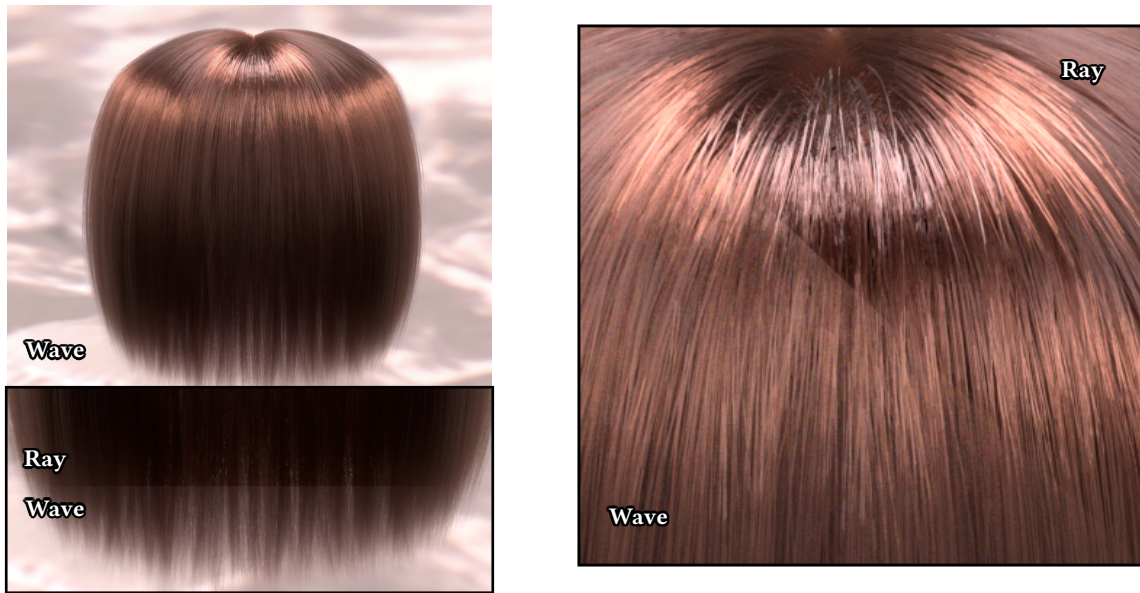

Fig. 15. This figure shows renderings of a head of elliptical red hair lit by an environment light. The aspect ratio of these elliptical fibers is 1.6 and for the wave model, we set the ellipse semi-major and semi-minor axes to be $16\mu m$ and $10\mu m$. We show the full-scale render using our wave BCSDF on the top left. On the bottom left, we zoom in on hair ends and show the comparison between the ray and the wave renders. On the right, we zoom in near the root of hair. Comparing to the ray render, the wave render has different highlight patterns and a softer appearance.

8.4 Performance

We report the wave simulation time on an 8-core Intel i9-9900K machine (Table 1). This table contains the simulation information for generating the azimuthal scattering distribution of 9 different kinds of cross sections. For circular fibers, we compute their azimuthal functions using the Mie solution and for non-circular fibers, their azimuthal functions are calculated using the BEM based simulator.

The number of ϕ_r samples is 360 for all examples except for the circular cross section with $100\mu m$ radius, where we use 3600 samples. We use 100 θ_i samples for all examples.

We report rendering time on the same machine (Table 2). We use spectral rendering with 50 wavelengths for both the ray-based and the wave-based BCSDF. We use wavelength-independent sampling for both the ray-based and the wave-based model.

Table 1. Simulation time.

	Circle 1	Circle 2	Circle 3	Ellipse 1	Ellipse 2	Ellipse 3	Polyester 1	Polyester 2	Silk
Radius* (μm)	1	10	100	1.6	16	19	5	5	5.6
Segment#	-	-	-	300	2000	2375	675	804	629
Matrix size	-	-	-	1200^2	8000^2	9500^2	2700^2	3216^2	2516^2
ϕ_i samples	1	1	1	90	90	90	360	360	360
Spectral samples	50	100	500	50	100	100	50	50	50
Time	5s	19s	1.1h	1.3h	77.3h	91.8h	12.1h	15.1h	13.0h
$\max(C_e/C_g)^*$	6.0	3.0	2.2	6.0	2.5	2.5	2.7	2.8	2.5

* Radius is defined as the max distance between a point on the cross section contour to the center; the center is computed by averaging all the vertex positions.

* The last row reports the maximal ratio of the effective to the geometric cross section over incident direction and wavelength. The values of Circle 1 and Ellipse 1 were clamped.

Fig. 16. In this figure, we showcase an animal fur rendering. The hamster fur is textured using six kinds of elliptical fibers with different colors The semi-major and semi-minor axes of the fiber are $16\mu m$ and $10\mu m$. On the left, we split the full-scale render into two halves, where the bottom left half is rendered using the ray method and the top right half is rendered using our wave BCSDF. On the right, we display zoom-in renders that interleave ray (odd squares) and wave (even squares) results in a checkerboard pattern. The wave result has softer highlights and has more overall translucency.

Grid (x, y)
if x+y is odd: ray
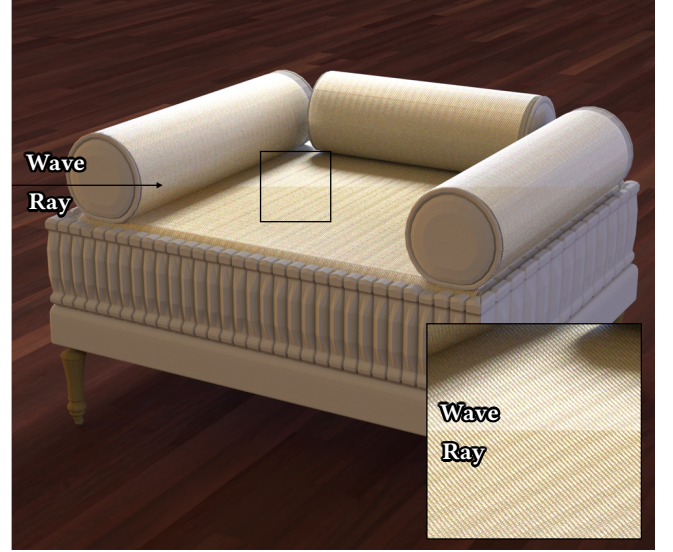if x+y is even: wave

Fig. 17. This figure shows a sofa scene, where the top surface of the sofa and the side surfaces of the three cylinders are made of silk. The SEM of this silk fiber is shown in figure 7 (a) and the ϕ_i vs. ϕ_r plot of the azimuthal scattering function can be found in figure 6. We compared the ray result and the wave result by splitting the images (regular and zoom-in) into two halves: the top halves are rendered using our wave BCSDF while the bottom halves are rendered using the ray method. We observe stronger highlights and some color shifts in the wave render.

9 DISCUSSION AND CONCLUSION

This paper introduces the first wave optics based fiber scattering model. Under the assumption that the fiber does not have variations along the fiber axis locally, we use this symmetry to decompose the 3D fiber scattering problem into an easier 2.5D problem. We build wave-based azimuthal scattering functions by numerically solving Maxwell's equations with a boundary element method and compute the azimuthal distribution from the simulated scattered fields. We integrate our new fiber scattering model into a modern renderer by precomputing the azimuthal function used along with longitudinal functions from existing models. We show that our wave-based fiber scattering model can render diffraction and interference effects that cannot be handled by conventional ray optics models and demonstrate highlight prediction differences between the ray optics and the wave optics models. This work is the first step towards more general wave optics fiber scattering models and there are many exciting future directions we would like to pursue to improve the current solution.

Generalization to full 3D. Our current work makes use of 2.5D wave simulation, which requires the assumption that the BCSDF can be decomposed into longitudinal and azimuthal scattering functions and that we keep the ray-based longitudinal function. In the future

Table 2. Rendering time.

Fig.	Method	Resolution	Spp	Time
1 (b)	Wave	800×800	512	38min
1 (c)	Ray	800×800	512	32min
4	Ray	400×400	64	18s
4	Wave	400×400	64	28s*
8 (a)	Ray	400×400	64	70min
8 (b)	Wave	400×400	64	82min
8 (c)	Wave	400×400	64	80min
13	Ray	400×400	64	22s*
13	Wave	400×400	64	28s*
14	Ray	1600×900	192	22.7h
14	Wave	1600×900	192	22.9h
15	Ray	800×800	128	8.0h
15	Wave	800×800	128	8.0h
16	Ray	1200×1440	128	32.0h
16	Wave	1200×1440	128	33.2h
17	Ray	1400×1400	128	16.9
17	Wave	1400×1400	128	17.0h

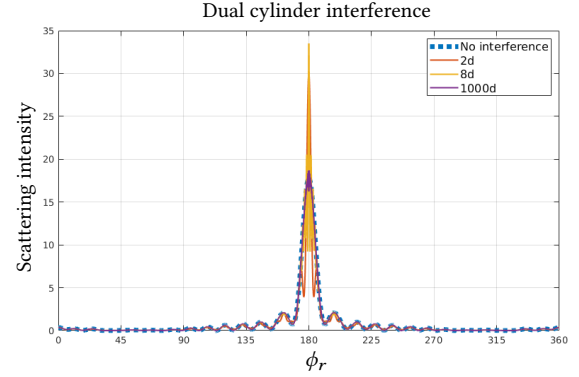* Rendering time is averaged across the wave/ray renders in that figure.

Fig. 18. This figure plots the wave-optics scattering from pairs of cylinders at various separation distances (2, 8, 1000 diameters) and compares them to our approximation which neglects inter-fiber interference effects. The closely spaced fibers exhibit high-frequency angular oscillations that our method does not capture, but the scattering pattern is otherwise similar and converges to our approximation as the cylinder distance increases.

work, we would like to generalize the current work to a full 3D wave model, which can potentially reveal other effects caused by longitudinal irregularity. A more general solution would involve upgrading our current simulator to 3D and solving the 3D boundary integral equation problem. As the dimension increases, we might need other acceleration methods such as the multilevel fast multipole algorithm (MLFMA) [Song et al. 1997], and compression schemes to keep the memory usage and running time reasonable. This generalization would remove the no cuticle scale assumption and also the longitudinal and azimuthal separation assumption.

Individual fiber assumption. Our method assumes that the scattering BCSDF for each fiber can be estimated independently of its surroundings. However, this neglects the interference effects that can occur between fibers when they are closely spaced. To illustrate this effect, we simulated the scattering from pairs of randomly-positioned circular lossless parallel cylinders with $1\mu m$ radii using μ-diff [Thierry et al. 2015]. Figure 18 shows the results for inter-cylinder distances of $4\mu m$, $16\mu m$ and $2000\mu m$ averaged over 10000 random configurations and compares them to our approximation without inter-cylinder interference. We observe that the dual cylinder results contain additional high frequency interference patterns, but are otherwise broadly similar to our no-interference approximation and converge to it as the distance between the cylinders increases. Note that we omit plotting the exact forward direction. Previous studies [Mishchenko et al. 2007, 2002] have shown that the exact forward-scattering direction is unique in that the phase shift is the same irrespective of the specific particle positions and constructive interference causes a strong forward-scattering enhancement.

Precomputation cost and storage. We reported the simulation time in Section 8.4 and storage cost in Section 6. Besides the acceleration methods we described in 6, we can further accelerate the simulation by adapting the simulator to be GPU based. We would also like to lower the storage cost of the wave-based azimuthal function

tables. We can compress the tables by fitting analytic functions to the distribution or applying learning techniques.

ACKNOWLEDGMENTS

REFERENCES

Carlos Aliaga, Carlos Castillo, Diego Gutierrez, Miguel A Otaduy, Jorge Lopez-Moreno, and Adrian Jarabo. 2017. An appearance model for textile fibers. In *Computer Graphics Forum*, Vol. 36. Wiley Online Library, 35–45.

DEv Amos. 1986. Algorithm 644: A portable package for Bessel functions of a complex argument and nonnegative order. *ACM Transactions on Mathematical Software (TOMS)* 12, 3 (1986), 265–273.

Armata. 2019a. IridescentWeb. https://www.flickr.com/photos/marianna_armat/40117157923/in/photostream/.

Marianna Armata. 2019b. *Marianna Armata.* www.passionatephotos.net.

K Murugesh Babu. 2018. *Silk: processing, properties and applications.* Woodhead Publishing.

Chen Bar, Marina Alterman, Ioannis Gkioulekas, and Anat Levin. 2019. A Monte Carlo framework for rendering speckle statistics in scattering media. *ACM Transactions on Graphics (TOG)* 38, 4 (2019), 1–22.

Petr Beckmann and Andre Spizzichino. 1987. The scattering of electromagnetic waves from rough surfaces. *Norwood, MA, Artech House, Inc., 1987, 511 p.* (1987).

Laurent Belcour and Pascal Barla. 2017. A practical extension to microfacet theory for the modeling of varying iridescence. *ACM Transactions on Graphics (TOG)* 36, 4 (2017), 65.

Craig F Bohren and Donald R Huffman. 2008. *Absorption and scattering of light by small particles.* John Wiley & Sons.

Max Born and Emil Wolf. 1999. Principles of optics, Chapter 1.

Matt Jen-Yuan Chiang, Benedikt Bitterli, Chuck Tappan, and Brent Burley. 2015. A Practical and Controllable Hair and Fur Model for Production Path Tracing. In *ACM SIGGRAPH 2015 Talks (SIGGRAPH '15).* Association for Computing Machinery, New York, NY, USA, Article Article 23, 1 pages. https://doi.org/10.1145/2775280.2792559

Eugene d'Eon, Guillaume Francois, Martin Hill, Joe Letteri, and Jean-Marie Aubry. 2011. An Energy-conserving Hair Reflectance Model. In *Proceedings of the Twenty-second Eurographics Conference on Rendering (EGSR '11).* Eurographics Association, Aire-la-Ville, Switzerland, Switzerland, 1181–1187. https://doi.org/10.1111/j.1467-8659.2011.01976.x

Eugene d'Eon, Steve Marschner, and Johannes Hanika. 2014. A fiber scattering model with non-separable lobes.. In *SIGGRAPH Talks*. 46–1.

Zhao Dong, Bruce Walter, Steve Marschner, and Donald P. Greenberg. 2016. Predicting Appearance from Measured Microgeometry of Metal Surfaces. *ACM Trans. Graph.* 35, 1, Article Article 9 (Dec. 2016), 13 pages. https://doi.org/10.1145/2815618

Joey Dumont and Denis Gagnon. 2013. Compless_Bessel. https://blog.joey-dumont.ca/complex_bessel/.

Jeppe Revall Frisvad, Niels Jørgen Christensen, and Henrik Wann Jensen. 2007. Computing the scattering properties of participating media using Lorenz-Mie theory. In *ACM SIGGRAPH 2007 papers*. 60–es.

Walton C Gibson. 2014. *The method of moments in electromagnetics*. Chapman and Hall/CRC.

Jay S Gondek, Gary W Meyer, and Jonathan G Newman. 1994. Wavelength dependent reflectance functions. In *Proceedings of the 21st annual conference on Computer graphics and interactive techniques*. 213–220.

Gaël Guennebaud, Benoît Jacob, et al. 2010. Eigen v3. http://eigen.tuxfamily.org.

RF Harrington and Time-Harmonic Electromagnetic Fields. 1961. pp. 460-463.

James E Harvey. 1979. Fourier treatment of near-field scalar diffraction theory. *American Journal of Physics* 47, 11 (1979), 974–980.

Xiao D He, Kenneth E Torrance, Francois X Sillion, and Donald P Greenberg. 1991. A comprehensive physical model for light reflection. In *ACM SIGGRAPH computer graphics*, Vol. 25. ACM, 175–186.

P Huddleston, L Medgyesi-Mitschang, and J Putnam. 1986. Combined field integral equation formulation for scattering by dielectrically coated conducting bodies. *IEEE transactions on antennas and propagation* 34, 4 (1986), 510–520.

Kane Yee. 1966. Numerical solution of initial boundary value problems involving Maxwell's equations in isotropic media. *IEEE Transactions on Antennas and Propagation* 14, 3 (May 1966), 302–307.

Pramook Khungurn and Steve Marschner. 2017. Azimuthal Scattering from Elliptical Hair Fibers. *ACM Trans. Graph.* 36, 2, Article Article 13 (April 2017), 23 pages. https://doi.org/10.1145/2998578

Karl S Kunz and Raymond J Luebbers. 1993. *The finite difference time domain method for electromagnetics*. CRC press.

Young-Seak Lee, Yulia V Basova, Dan D Edie, Laura K Reid, Steven R Newcombe, and Seung-Kon Ryu. 2003. Preparation and characterization of trilobal activated carbon fibers. *Carbon* 41, 13 (2003), 2573–2584.

Tomas Linder. 2014. *Light scattering in fiber-based materials: a foundation for characterization of structural properties*. Ph.D. Dissertation. Luleå tekniska universitet.

Augustus Edward Hough Love. 1901. I. The integration of the equations of propagation of electric waves. *Philosophical Transactions of the Royal Society of London. Series A, Containing Papers of a Mathematical or Physical Character* 197, 287-299 (1901), 1–45.

Stephen R. Marschner, Henrik Wann Jensen, Mike Cammarano, Steve Worley, and Pat Hanrahan. 2003. Light Scattering from Human Hair Fibers. *ACM Trans. Graph.* 22, 3 (July 2003), 780–791. https://doi.org/10.1145/882262.882345

Michael I Mishchenko, Li Liu, Daniel W Mackowski, Brian Cairns, and Gorden Videen. 2007. Multiple scattering by random particulate media: exact 3D results. *Optics Express* 15, 6 (2007), 2822–2836.

Michael I Mishchenko, Larry D Travis, and Andrew A Lacis. 2002. *Scattering, absorption, and emission of light by small particles*. Cambridge university press.

A Musbach, GW Meyer, F Reitich, and SH Oh. 2013. Full wave modelling of light propagation and reflection. In *Computer Graphics Forum*, Vol. 32. Wiley Online Library, 24–37.

Matt Pharr and Greg Humphreys. 2010. *Physically Based Rendering, Second Edition: From Theory To Implementation* (2nd ed.). Morgan Kaufmann Publishers Inc., San Francisco, CA, USA.

Rafael Piestun and David AB Miller. 1999. Degrees of freedom of an electromagnetic wave. In *18th Congress of the International Commission for Optics*, Vol. 3749. International Society for Optics and Photonics, 110–111.

Andrew J Poggio and Edmund K Miller. 1970. *Integral equation solutions of three-dimensional scattering problems*. MB Assoc.

Thomas Rylander, Pär Ingelström, and Anders Bondeson. 2012. *Computational electromagnetics*. Springer Science & Business Media.

Iman Sadeghi, Heather Pritchett, Henrik Wann Jensen, and Rasmus Tamstorf. 2010. An artist friendly hair shading system. *ACM Transactions on Graphics (TOG)* 29, 4 (2010), 56.

Jan Schäfer. Retrieved May 20, 2020. MatScat. https://www.mathworks.com/matlabcentral/fileexchange/36831-matscat, MATLAB Central File Exchange..

J Schäfer, S-C Lee, and A Kienle. 2012. Calculation of the near fields for the scattering of electromagnetic waves by multiple infinite cylinders at perpendicular incidence. *Journal of Quantitative Spectroscopy and Radiative Transfer* 113, 16 (2012), 2113–2123.

Jan-Patrick Schäfer. 2011. *Implementierung und Anwendung analytischer und numerischer Verfahren zur Lösung der Maxwellgleichungen für die Untersuchung der Lichtausbreitung in biologischem Gewebe*. Ph.D. Dissertation. Verlag nicht ermittelbar.

SA Schelkunoff. 1936. Some equivalence theorems of electromagnetics and their application to radiation problems. *The Bell System Technical Journal* 15, 1 (1936), 92–112.

Brian E Smits and Gary W Meyer. 1992. Newton's colors: simulating interference phenomena in realistic image synthesis. In *Photorealism in Computer Graphics*. Springer, 185–194.

Jiming Song, Cai-Cheng Lu, and Weng Cho Chew. 1997. Multilevel fast multipole algorithm for electromagnetic scattering by large complex objects. *IEEE Transactions on Antennas and Propagation* 45, 10 (1997), 1488–1493.

Jos Stam. 1999. Diffraction shaders. In *Siggraph*, Vol. 99. 101–110.

Allen Taflove and Susan C Hagness. 2005. *Computational electrodynamics: the finite-difference time-domain method*. Artech house.

B. Thierry, X. Antoine, C. Chniti, and H. Alzubaidi. 2015. μ-diff: An open-source Matlab toolbox for computing multiple scattering problems by disks. *Computer Physics Communications* 192 (2015), 348 – 362. https://doi.org/10.1016/j.cpc.2015.03.013

Antoine Toisoul and Abhijeet Ghosh. 2017. Practical acquisition and rendering of diffraction effects in surface reflectance. *ACM Transactions on Graphics (TOG)* 36, 5 (2017), 1–16.

RK Varshney, VK Kothari, and S Dhamija. 2011. Influence of polyester fibre fineness and cross-sectional shape on low-stress characteristics of fabrics. *The Journal of the Textile Institute* 102, 1 (2011), 31–40.

Wall. 2011. Iridescence in a Dandelion Seed Head. https://epod.usra.edu/blog/2011/05/iridescence-in-a-dandelion-seed-head.html.

Sebastian Werner, Zdravko Velinov, Wenzel Jakob, and Matthias B Hullin. 2017. Scratch iridescence: Wave-optical rendering of diffractive surface structure. *ACM Transactions on Graphics (TOG)* 36, 6 (2017), 1–14.

Te-Kao Wu and L Tsai. 1977. Scattering by arbitrarily cross-sectioned layered, lossy dielectric cylinders. *IEEE Transactions on Antennas and Propagation* 25, 4 (1977), 518–524.

Ling-Qi Yan, Miloš Hašan, Bruce Walter, Steve Marschner, and Ravi Ramamoorthi. 2018. Rendering Specular Microgeometry with Wave Optics. *ACM Trans. Graph.* 37, 4, Article 75 (July 2018), 10 pages. https://doi.org/10.1145/3197517.3201351

Ling-Qi Yan, Henrik Wann Jensen, and Ravi Ramamoorthi. 2017. An Efficient and Practical near and Far Field Fur Reflectance Model. *ACM Trans. Graph.* 36, 4, Article 67 (July 2017), 13 pages. https://doi.org/10.1145/3072959.3073600

Ling-Qi Yan, Chi-Wei Tseng, Henrik Wann Jensen, and Ravi Ramamoorthi. 2015. Physically-Accurate Fur Reflectance: Modeling, Measurement and Rendering. *ACM Trans. Graph.* 34, 6, Article Article 185 (Oct. 2015), 13 pages. https://doi.org/10.1145/2816795.2818080

Arno Zinke, Martin Rump, Tomás Lay, Andreas Weber, Anton Andriyenko, and Reinhard Klein. 2009. A Practical Approach for Photometric Acquisition of Hair Color. In *ACM SIGGRAPH Asia 2009 Papers (SIGGRAPH Asia '09)*. Association for Computing Machinery, New York, NY, USA, Article Article 165, 9 pages. https://doi.org/10.1145/1661412.1618511

Arno Zinke and Andreas Weber. 2007. Light scattering from filaments. *IEEE Transactions on Visualization and Computer Graphics* 13, 2 (2007), 342–356.